JACS
JOURNAL OF THE AMERICAN CHEMICAL SOCIETY
pubs.acs.org/JACS
Article

Orbital-Resolved Stepwise Single-Electron Capture Dynamics in a Single Fullerene

Zezhou Yang,[‖] Boyu Wang,[‖] Xinmiao Xie,[‖] Hanqiu Nie,[‖] Jianning Zhang,[‖] Panfeng Chuai, Jie Hao, Wenlong Cai, Zhiheng Yang, Chunyan Gao, Fanyang Mo,* Zujin Shi,* Jinying Wang,* Chuancheng Jia,* and Xuefeng Guo*

Cite This: https://doi.org/10.1021/jacs.5c08782

ABSTRACT: Fullerenes (C_{60}), characterized by their unique cage-like structure and strong electron-accepting properties, have found extensive applications in organic electronics, photovoltaics, and photocatalysis. At the same time, they are gaining more attention in emerging fields, such as spintronics and quantum technologies. However, precise manipulation of the electron behavior within C_{60}, particularly the capture of varying numbers of electrons by an individual C_{60} molecule, remains a formidable challenge. In this study, we realize the accurate monitoring of the sequential single-electron capture process of a single C_{60} molecule bound between graphene electrodes. Real-time current measurements reveal four distinct charge states with specific Frontier orbitals under cryogenic conditions (2 K), corresponding to the capture of 0, 1, 2, and 3 electrons. Theoretical calculations suggest that the ability of C_{60} to accept multiple electrons originates from the coupling between molecular vibrations and transported electrons. Furthermore, the effect of the electric field on the local density of states highlights its crucial role in the precise control of electron capture on a single C_{60}. These findings provide useful insights into the dynamic evolution of stepwise electron capture in fullerene and demonstrate the potential of fullerene-based materials in molecular electronics and quantum technologies.

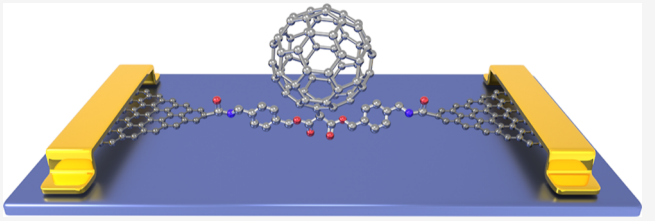

INTRODUCTION

Precise manipulation of the electron dynamics within molecular systems is a pivotal challenge for advancing next-generation electronics, optoelectronic devices, and quantum information technologies.[1−4] Among diverse molecular systems, fullerenes, such as C_{60} and its derivatives, have attracted significant interest due to their unique cage-like structure, exceptional electronic properties, and inherent tunability.[5−8] In particular, C_{60} possesses the dual capacity for both electron acceptance and donation and exhibits the remarkable stability and a relatively simple electronic configuration, which renders it highly promising for applications in organic photovoltaics,[9,10] photocatalysis,[11−13] molecular spintronics,[14] and quantum information.[15,16] Therefore, the ability to precisely manipulate the individual electron behavior of C_{60} is crucial for realizing its widespread application in these fields. Sequential and precise control of electrons would substantially enhance the device performance and functionality, thereby facilitating efficient energy conversion,[17] data storage,[18] and even the realization of quantum computing.[19] As a result, realizing sequential and precise control of single electrons in fullerenes is not merely a technical challenge but also a critical step toward unlocking their broad application potential in molecular electronics and related fields.

The existing methodologies for electron regulation currently comprise doping,[20] electrochemical approaches,[21] and electrical gate control.[22] Doping, which induces electron transfer through the introduction of foreign atoms, is inherently stochastic and irreversible, thereby impeding precise control of electron dynamics.[23] Electrochemical approaches, which is capable of facilitating electron transfer in solution, are similarly constrained by their inability to achieve stepwise electron capture and release at the single-molecule level.[24] These limitations are exacerbated by the challenges associated with macroscopic measurements, which are often compromised by electric field interference, Coulomb shielding effects, and the inherent inability to monitor the real-time evolution of the electron states. The advent of single-molecule techniques offers a powerful means for precisely manipulating the electron behavior within individual molecules, effectively bridging the gap associated with the limitations of macroscopic approaches.[25−27] Single-molecule devices based on C_{60} have already demonstrated several remarkable physical phenomena, including the Kondo effect,[28] quantum phase transitions,[29] superconductivity,[30] and negative differential resistance.[31] Notably, the regulation of C_{60} valence states via

Received: May 24, 2025
Revised: July 29, 2025
Accepted: August 14, 2025

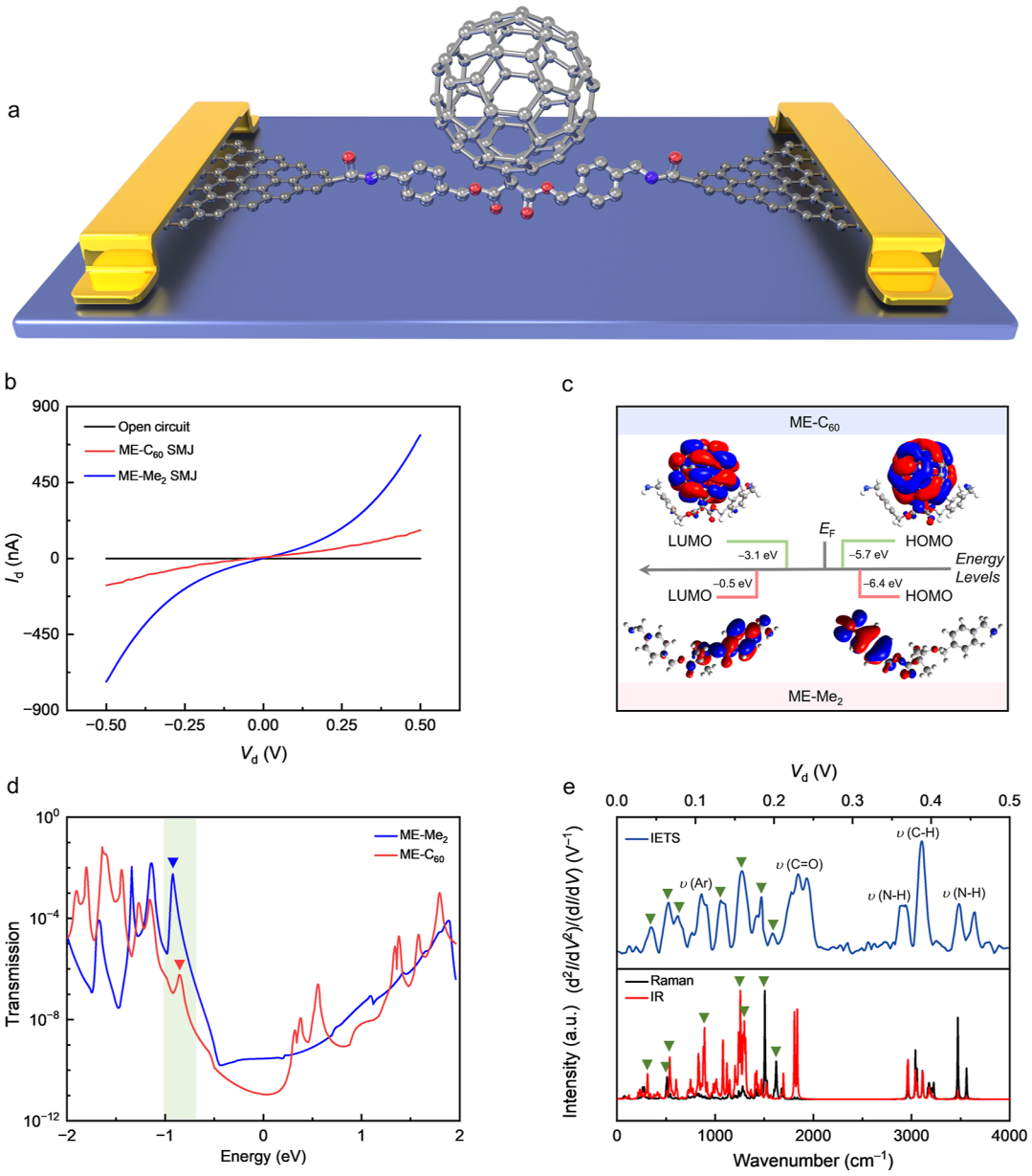

Figure 1. Structure and characterization of single-molecule devices. (a) Schematic diagram of a ME-C_{60}-based single-molecule junction. (b) $I-V$ characteristics before (black line) and after (red line and blue line) incorporating individual ME-C_{60} and ME-Me_2 molecules into a graphene nanogap at room temperature, respectively. (c) Optimized molecular orbitals of ME-C_{60} and ME-Me_2. (d) Transmission spectra of the ME-C_{60}-SMJ (red) and ME-Me_2-SMJ (blue). *p*-HOMOs are marked with downward triangles. (e) High-resolution IETS (plotted using Bezier curves) (top) for a ME-C_{60}-based SMJ measured by a lock-in the second-harmonic technique at 2 K with an alternating-current modulation of 15 mV (root-mean-square value) at a frequency of 311 Hz, accompanied by corresponding predicted IR and Raman spectra (bottom).

solid-gate control has been extensively studied as a prototype for single-molecule transistors.[26,30,32] Although electrochemical gating allows for continuous and reversible control of the charge state by adjusting the gate voltage to modify the redox state of molecules in the electrolyte, the use of liquid electrolytes inherently limits their operating temperature range due to the risk of freezing at cryogenic temperatures and volatility at elevated temperatures.[33−35] These seminal investigations have collectively heightened the interest in understanding electron capture within manipulable single-molecule systems. However, direct monitoring of electron capture dynamics in C_{60} and the realization of sequential electronic regulation remain highly challenging, hindering further advancements in fullerene-based electronics and spintronics.

Although previous studies have investigated gate-controlled charge trapping[26] and inclusion complex migration[36,37] in fullerene-based single-molecule junctions, the dynamics of charge trapping and its continuous modulation remain unexplored. This gap can be attributed to the reliance on noncovalent contacts between C_{60}[32,38] or conjugated systems[39] and the electrodes in these junctions, which inherently compromise the device stability and reproducibility. Herein, static graphene-molecule-graphene single-molecule junctions (GMG-SMJs) covalently integrated with a single C_{60} are constructed, enabling real-time, high-resolution electrical measurements, and precise control of the electron capture behavior. This architecture of single C_{60} junctions allows for a systematic investigation into the influence of an external electric field (bias voltage) on the

https://doi.org/10.1021/jacs.5c08782
J. Am. Chem. Soc. XXXX, XXX, XXX−XXX

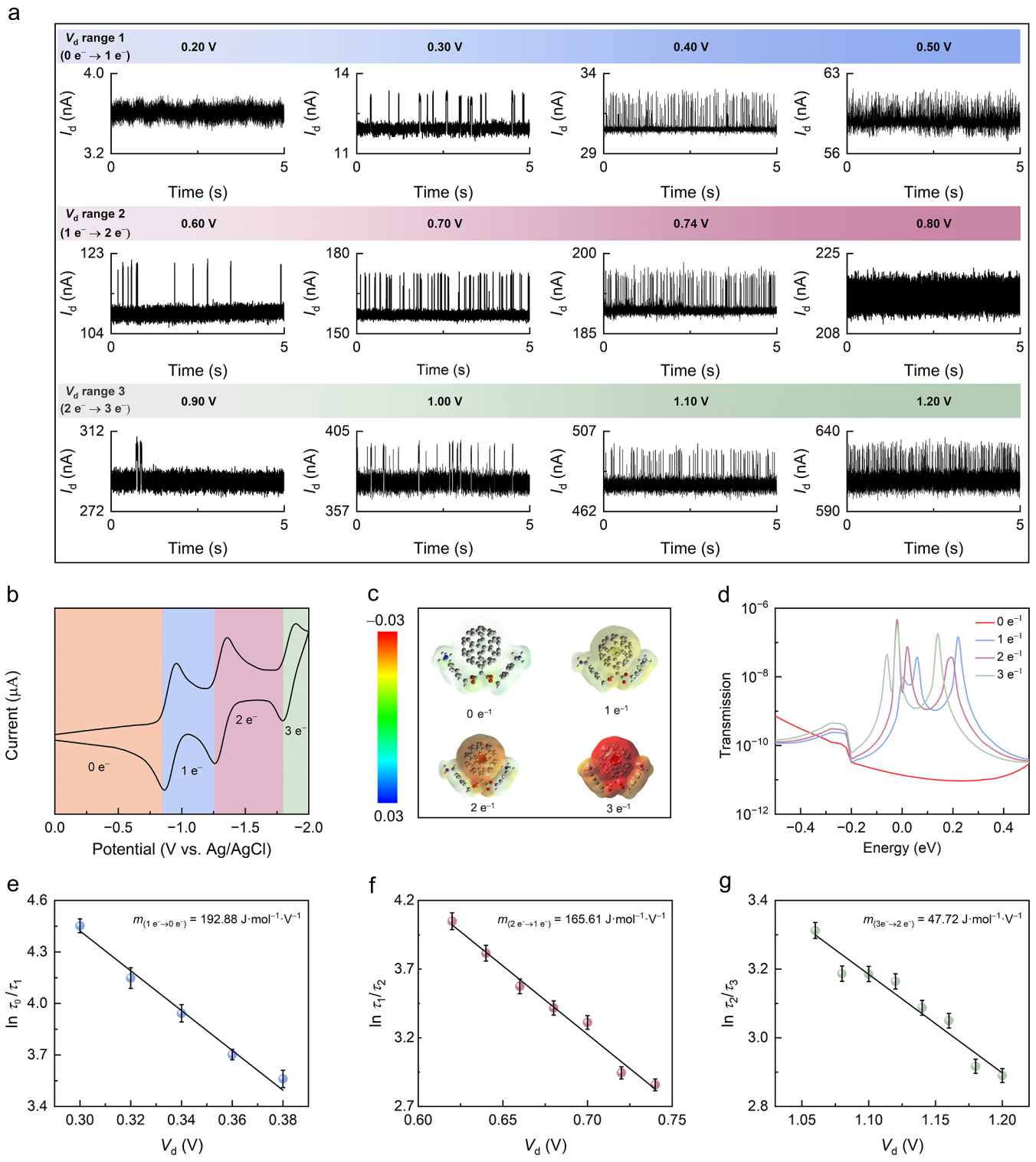

Figure 2. Bias voltage-dependent measurements and signal analyses of a single ME-C_{60} junction. (a) I−t curves of a ME-C_{60} junction at 2 K under increasing V_d from 0.20 to 1.20 V. (b) CV characteristics of the molecular precursor ME-C_{60}. (c) Calculated electrostatic potential maps of ME-C_{60} with captured electrons in different numbers. (d) Transmission spectra of a ME-C_{60} junction with different electronic states at zero bias. (e−g) Voltage-dependent thermodynamic parameters of electronic state transitions from 1 e^- to 0 e^-, 2 e^- to 1 e^-, and 3 e^- to 2 e^- in three V_d windows (0.30−0.50 V, 0.50−0.80 V, and 0.80−1.20 V).

electronic states of C_{60}, as well as the interplay between electron transfer and the molecular structure. By leveraging the coupling between electric field-regulated molecular vibrational modes and thermally activated electron transport, this architecture provides a platform to dynamically tune the sequential electron capture, release, and transport in C_{60} from a single-molecule perspective. The strategic integration of graphene electrodes with covalently bound C_{60} not only establishes a robust framework for studying electron−molecule interactions but also underscores the potential of rationally designed single-

https://doi.org/10.1021/jacs.5c08782
J. Am. Chem. Soc. XXXX, XXX, XXX−XXX

molecule junctions in advancing quantum information science and practically implementing single-electron manipulation technologies.

RESULTS AND DISCUSSION

Preparation and Characterization of ME-C_{60}-Based GMG-SMJs. Fullerene possesses conjugated orbitals distributed across the entire spherical structure. These partially filled Frontier orbitals allow fullerene to act as an electron acceptor and donor. For example, the electronic states of C_{60} can be effectively modulated by external stimuli, such as electric fields, making it an ideal model system for studying the intricate electron transport and charge trapping.[26] Here, a single-molecule device is fabricated by integrating a dimethylmalonate-fullerene derivative (ME-C_{60}) into graphene electrodes via covalent bonding at both ends of the dimethylmalonate (Figure 1a). The amino groups at the ends of ME-C_{60} form stable amide bonds with the carboxyl groups on graphene, ensuring a high level of stability and reliability for the single-molecule device. This one-step protocol is used to directly connect ME-C_{60} between graphene electrodes, rather than first attaching dimethylmalonate followed by C_{60} modification, thereby ensuring that C_{60} is positioned at a designated site. The synthesis and characterization of both the ME-C_{60} and methylated derivative diethyl 2,2-dimethylmalonate (ME-Me_2) (as a control system) are shown in the Supporting Information (Figures S1−S9). Further details of device fabrication are provided in the Methods section (Figures S10−S12).

To check the connection between ME-C_{60} and graphene electrodes as well as the consequent formation of a closed-loop structure, current−voltage (I−V) measurements of the device at different stages are conducted. After successfully connecting a single ME-C_{60} molecule, the current significantly increases from the fA−pA to the nA range at the same bias voltage (0.5 V) (Figures 1b and S13). The dramatic rise in current indicates the successful construction of single ME-C_{60} junctions. A binomial distribution analysis (see details in Supporting Information Section S4) shows that approximately 35% of the devices exhibit successful connection, and the ratio of single-molecule-connected devices to the overall reconnected devices is ∼83%. The conductance of ME-C_{60} is significantly lower than that of ME-Me_2 (Figures 1b and S14), probably due to the localization of molecular Frontier orbitals within the C_{60} cage for ME-C_{60}, whereas the orbitals of ME-Me_2 are distributed across the entire molecular backbone (Figure 1c). The transmission spectrum is also calculated to confirm the conductance order at the Fermi level (ME-Me_2 > ME-C_{60}) (Figure 1d). Despite the energy levels of ME-C_{60} being more closely aligned with the Fermi level compared to those of ME-Me_2, the presence of localized orbitals reduces the transmission efficiency of the transport channel. The stronger coupling between ME-Me_2 and the electrodes compared to ME-C_{60} further leads to higher molecular conductance. Furthermore, inelastic electron tunneling spectroscopy (IETS) is performed on the ME-C_{60} single-molecule device (Figure 1e). By combining the simulated IR and Raman spectra of ME-C_{60}, the peaks at ∼224 mV (ν(C═O)) and ∼438 mV (ν(N−H)) are ascribed to the amide bond, respectively, proving the formation of a molecular connection. The peaks marked by green triangles indicate several vibrational modes generated by C_{60}, confirming the successful fabrication of the device.

Electronic State Transitions of C_{60} at Cryogenic Temperatures under Bias Voltages. Cryogenic temperatures typically play a crucial role in achieving resonant tunneling and stabilizing transient charge states under high bias voltages,[40,41] due to several factors, including the reduction of thermal broadening of energy levels, suppression of inelastic tunneling noises, enhanced structural stability of molecular junctions, and decreased thermal-activation-driven decay. To show the influence of temperature on molecular conductance, I−V measurements are carried out at different temperatures ranging from 2 to 300 K (Figure S15). The results indicate that the current increases with the rising temperature, which is consistent with previous studies.[42,43] To elucidate the sequential electron capture behavior of ME-C_{60}-based single-molecule devices, current−time (I−t) measurements are carried out at a low temperature of 2 K under different bias voltages (V_d) ranging from 0.20 to 1.20 V (Figures 2a and S16, S19, and S22). The bias voltage can incrementally achieve energy level alignment between the molecule and distinct electrodes through continuously adjusting the Fermi level difference between the electrodes, thereby enabling facile charge injection into molecules. This optimal V_d range is selected to guarantee the device reliability and achieve a high signal-to-noise ratio. Figure 2a shows that a single conductance state is observed when V_d is less than 0.20 V. As V_d increases, a new high-conductance state emerges, characterized by accelerated switching between the two distinct states and a growing prevalence of the high-conductance state. Upon reaching a V_d of 0.50 V, it is difficult to distinguish between high and low states based on the measured current levels due to the limitations of time resolution, and the low-conductance state with extremely short dwell times gradually disappears. As the V_d continues to increase, the second and third switching windows between high and low states emerge, following the same trend of increasing switching frequency within the range of 0.50−0.80 V and 0.80−1.20 V. In contrast, the ME-Me_2 control junctions always exhibit a single conductance state as V_d changes from 0.20 to 1.00 V at low temperatures (Figure S25), underscoring that the difference in the electrical conductance states within ME-C_{60}-based single-molecule devices can be predominantly attributed to the presence of the C_{60} functional center.

To unravel the mechanism behind the sequential change in molecular conductance across different bias windows in fullerene, macroscopic experiments combined with theoretical calculations are performed. Cyclic voltammetry (CV) measurements of the molecular precursor ME-C_{60} (Figure 2b) reveal that the fullerene derivative undergoes continuous redox reactions, driven by electron gain and loss in the range from 0 to −2 V, corresponding to four different electronic states. This suggests that the distinct V_d windows in I−t measurements of ME-C_{60}-based single-molecule devices are associated with the sequential electron capture behavior of C_{60}, and the switching between conductance states reflects the process of how C_{60} captures and releases electrons by V_d-governing electron injection. There is a difference between the bias window and the oxidation−reduction potential, which can be attributed to the average effect of the macroscopic system and the difference in the measurement environment. Assuming that the low-conductance state and high-conductance state correspond to the adjacent two electronic states of C_{60}, n e^- and $(n + 1)$ e^-, the following applies: in the first V_d window, the bistable states correspond to the 0 e^- and 1 e^- states; in the second V_d window, the bistable states correspond to the 1 e^- and 2 e^- states; and in the third V_d window, the bistable states correspond to the 2 e^- and 3 e^- states. The calculated electrostatic potential maps

https://doi.org/10.1021/jacs.5c08782
J. Am. Chem. Soc. XXXX, XXX, XXX−XXX

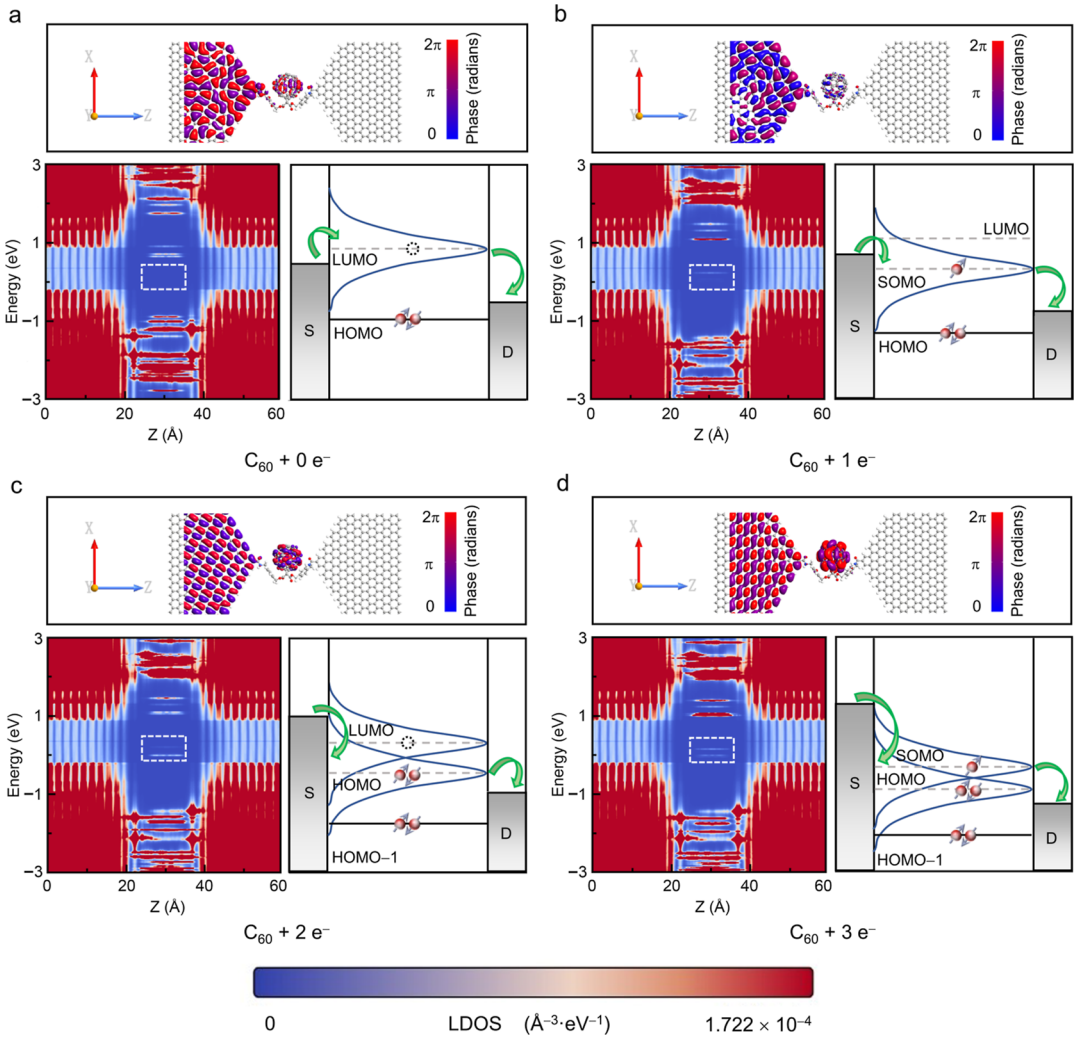

Figure 3. Energy level-dependent charge transport mechanism. (a–d) Local density of states (LDOS) of C_{60} in four different charge states, ranging from the neutral state (C_{60} + 0 e^- (a)) to increasingly charged states (C_{60} + 1 e^- (b), C_{60} + 2 e^- (c), and C_{60} + 3 e^- (d)) and corresponding energy–level diagrams. Top panel: Corresponding transmission eigenstates of the dominant transmission channel.

(Figure 2c) demonstrate that the captured electrons are localized on the C_{60} unit within the molecule to form different electronic states. The charge transport characteristics of ME-C_{60} junctions with varying electron charges are calculated under the Landauer framework to confirm our hypothesis. The neutral structure exhibits off-resonant transport characteristics in the low-bias region, resulting in a single low-conductance state when $V_d \leq 0.20$ V. Electron injection into C_{60} forms new transmission channels near the Fermi level, and the increasing electron capture shifts the transmission peaks leftward, demonstrating the conductance channels gradually entering the bias window (Figure 2d). Therefore, within the three V_d windows, a new high-conductance state can be observed as the V_d increases.

The dynamic evolution of stepwise electron capture in C_{60} is further analyzed by focusing on the I–t trajectories within three V_d windows (0.30–0.50 V, 0.50–0.80 V, and 0.80–1.20 V, respectively; further details are provided in Supporting Information 6, Figures S17 and S18, and S20, S21, S23 and S24). It is worth noting that the low-conductance state corresponds to a long dwell state, whereas the high-conductance state corresponds to a short dwell state at the beginning of the three V_d windows. The average lifetime of the low-conductance state progressively decreases as V_d increases in each V_d window.

The kinetic properties for the transition between the high and low states are obtained by applying the Eyring equations. Specifically, the Gibbs free energy of activation ($\Delta G^{\ddagger}$) for the high and low states transition substantially reduces with increasing electric fields across the three V_d windows. The change in the Gibbs free energy (ΔG^{θ}) (from $(n+1)$ e^- to n e^-) with the bias voltage can be defined as $-RT\ln K = \Delta G^{\theta} \approx m \cdot V_d + \Delta G_0$, where K is the equilibrium constant (K can be regarded as the ratio of the dwell times for the two-state switching, i.e., τ_0/τ_1, τ_1/τ_2 and τ_2/τ_3), m is the slope, V_d is the electric field strength, and ΔG_0 is the ΔG value when there is no electric field (Figure 2e–g). Herein, m can semiquantitatively reflect the impact of the electric field on the potential energy difference between different states.[25,44] Then, m is calculated as ~192.88 J·mol^{-1}·V^{-1}, ~165.61 J·mol^{-1}·V^{-1}, and ~47.72 J·mol^{-1}·V^{-1} corresponding to 1 $e^- \rightarrow$ 0 e^-, 2 $e^- \rightarrow$ 1 e^-, and 3 $e^- \rightarrow$ 2 e^-, respectively. As V_d increases in each window, the capture of a single electron is promoted, leading to the bistable switch shifting toward a high conductance state within the measurement bias range. Within three V_d windows, the value of m gradually decreases as V_d increases, indicating that the influence of the electric field on the electron-capturing ability is gradually weakening. The electric field enhancement can readily reduce the potential energy

https://doi.org/10.1021/jacs.5c08782
J. Am. Chem. Soc. XXXX, XXX, XXX–XXX

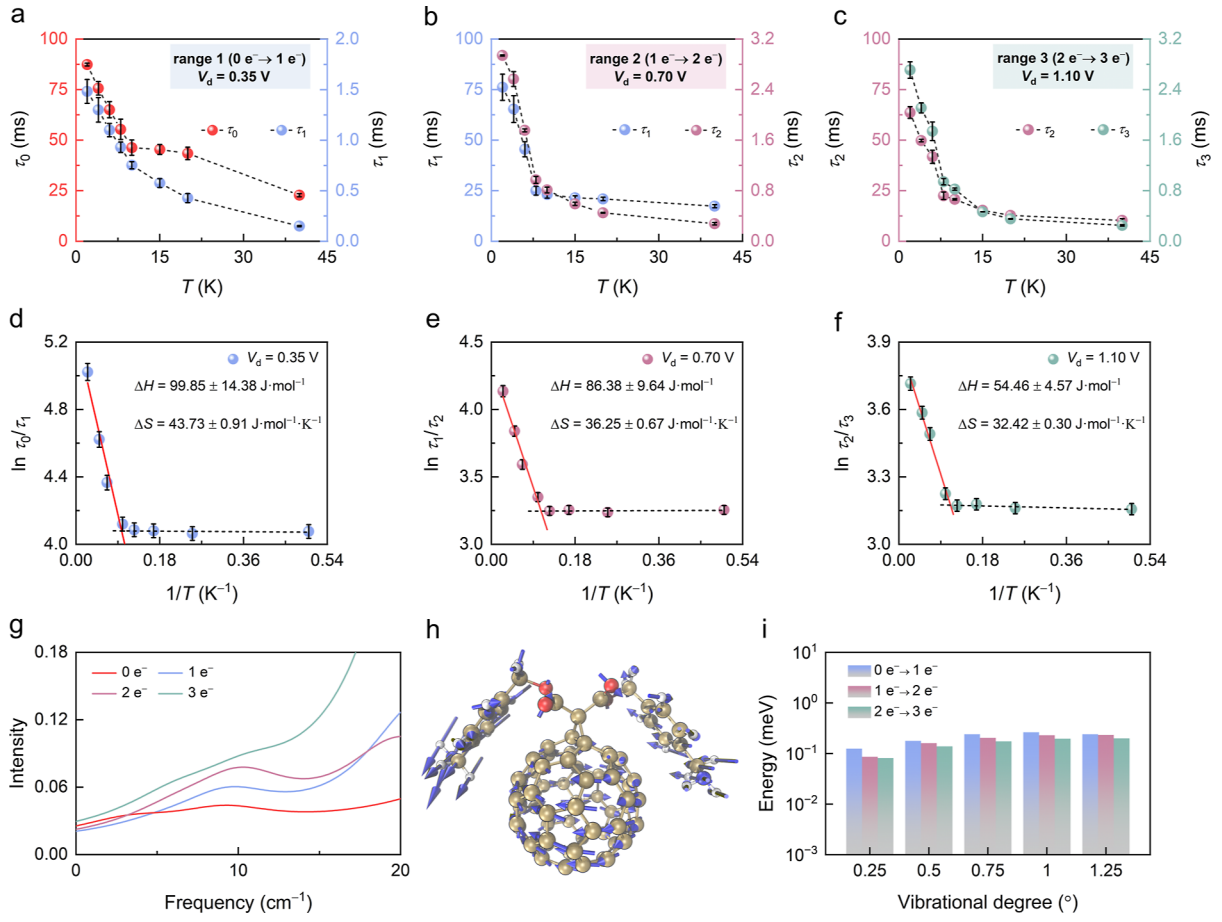

Figure 4. Mechanism for the charge transport transition. (a–c) Dwell time (τ) statistics extracted from single-exponential fits at temperatures ranging from 2 to 40 K under V_d values of 0.35, 0.70, and 1.10 V across three different V_d windows. (d–f) Temperature-dependent thermodynamic parameters of electronic state transitions from 1 e^- to 0 e^-, 2 e^- to 1 e^-, and 3 e^- to 2 e^- ranging from 2 to 40 K under V_d values of 0.35, 0.70, and 1.10 V across three different V_d windows. (g) Calculated vibrational spectra of four electronic states of C_{60}. (h) Activated vibrational modes of ME-C_{60}. (i) The potential energy as a function of vibrational degree for electronic states transition from 1 e^- to 0 e^-, 2 e^- to 1 e^-, and 3 e^- to 2 e^-.

difference between 1 e^- → 0 e^- and 2 e^- → 1 e^-, which is consistent with ΔG^{θ} calculations (m of 1 e^- → 0 e^- and 2 e^- → 1 e^- transport is much higher than that for 3 e^- → 2 e^-).

Analysis of Electronic State Transition Mechanism via Local Density of States. To further elucidate the transition mechanism of electronic states, we examine the local density of states (LDOS) of C_{60} in four different charge states, ranging from the neutral state (C_{60} + 0 e^-) to incrementally charged states (C_{60} + 1 e^-, C_{60} + 2 e^-, and C_{60} + 3 e^-), labeled as Figure 3a–d, respectively. The LDOS maps on the left of each subfigure depict the spatial distribution of electronic states along the z-axis of SMJs, revealing how the electronic structure evolves with the addition of an electron. On the right, the corresponding energy–level diagrams show the alignment of molecular orbitals relative to the source (S) and drain (D) electrodes, providing insights into the available conductive channels at each charge state.

The LDOS map shows that the molecular orbitals are localized at specific energy levels, suggesting weak coupling between the molecule and the electrode. In the neutral state of C_{60} (Figure 3a), the Frontier molecular orbitals are positioned on either side of the Fermi level, creating a transmission gap that limits electron tunneling between the source and drain electrodes. Consequently, neutral C_{60} exhibits a low conductance. As shown in Figure 3b, the injection of a single electron shifts the singly occupied molecular orbital (SOMO) closer to the Fermi level, introducing an additional conductive channel. This enhancement in charge transport is more clearly illustrated in the energy–level diagram, where the SOMO overlaps with the Fermi level, increasing the probability of electron tunneling and thereby boosting the overall conductance. In Figure 3c, the C_{60} molecule now accommodates two extra electrons, and multiple transport channels emerge near the Fermi level in the LDOS map. This electron injection enhances orbital coupling to enable more efficient electron transmission through the molecule, leading to a substantial improvement in the charge transport process. Figure 3d shows C_{60} in its triply charged state. In the energy–level diagram, both the highest occupied molecular orbital (HOMO) and SOMO states are positioned close to or at the Fermi level, as verified by the corresponding LDOS map. This maximal overlap results in optimal electron tunneling conditions, thereby significantly increasing the conductance of the system. The ability of C_{60} to accommodate and stabilize three additional electrons is directly linked to its improved transport characteristics as more electrons enable a greater number of channels for conduction. This explains the I–t results, where C_{60} with more electrons exhibits a higher conductance.

Temperature-Dependent Charge Transport Characteristics. To unveil the underlying mechanism governing the transition of distinct conductance states and electronic states of

https://doi.org/10.1021/jacs.5c08782
J. Am. Chem. Soc. XXXX, XXX, XXX–XXX

C_{60}, temperature-dependent $I-t$ measurements of single-ME-C_{60} junctions, ranging from 2 to 40 K, are carried out across three different V_d windows. As the temperature increases, the two conductance states exhibit reversible transitions under V_d values of 0.35, 0.70, and 1.10 V, accompanied by an increase in switching frequency. Lifetimes of the conductance states (τ) are obtained through statistical analyses of the $I-t$ data over 20 s by single-exponential fits. As shown in Figure 4a−c, the average lifetimes of the two conductance states progressively decrease as the temperature increases in each of the three windows. The statistics of dwell times at different temperatures across three different V_d windows are provided in Tables S1−S3. Using the Van't Hoff equation ($-RT\ln K = \Delta H - T\Delta S$), we can deduce the thermodynamic parameters of the transition between different electronic states. The relationship between $\ln K$ and $1/T$ shows no significant correlation below 10 K and an approximately linear correlation above 10 K (Figure 4d−f).

Previous studies have posited that the transition of molecular electronic transport from temperature-independent to temperature-dependent behaviors is likely closely associated with molecular vibrations.[42,43] To elucidate this correlation, we calculated the molecular vibrational spectra and vibrational modes. Figure 4g reveals that the vibrational spectra of C_{60} in distinct electronic states consistently exhibit prominent vibrational peaks near 7 cm^{-1}, which correspond to a transition temperature of 10 K. Notably, the vibrations are all characterized by the rotation of C_{60} relative to its molecular framework (Figure 4h), independent of the number of electrons in C_{60}. We consider that the observed temperature-dependent transition at 10 K across C_{60} in various electronic states can be explained well by the thermally induced vibration-assisted electron tunneling mechanism. In other words, at low temperatures (<10 K), the specific C_{60}-rotation modes are suppressed, resulting in no significant temperature dependence. As the temperature increases (>10 K), thermally induced vibrations of the C_{60} molecular framework facilitate electron tunneling, thereby increasing the probability of electron capture and generating a linear dependence on temperature. To achieve a more comprehensive understanding of the vibrationally assisted tunneling process, the energy profile associated with C_{60} vibrations is simulated through a small-range rotational motion. Figure 4i presents the relative energy variation, showing minimal differences between electronic states within a vibrational degree of ±1°, a range that remains thermally accessible at 10 K, consistent with experimental results. In addition, as the number of electrons captured by C_{60} increases, although the rotational vibrational modes remain largely invariant, the coupling between the molecular orbitals and electrodes is significantly enhanced. This augmented coupling leads to an increase in the vibrational-electronic coupling of C_{60}, thereby causing the enthalpy (ΔH) and entropy (ΔS) to decrease with the increasing electric field.

CONCLUSIONS

In summary, robust GMG-SMJs are fabricated with C_{60}, and real-time electrical measurements are performed to investigate the intricate processes involved in C_{60} electron transport and charge trapping. By applying electric fields, dynamic conversions between distinct electronic states of C_{60} (n e^- and $(n+1)$ e^-) are stimulated in three conductance windows at cryogenic temperatures, where electrons reside in different molecular orbitals, forming distinct conductance states. LDOS maps reveal how the electronic structure evolves with the addition of electrons from 0 to 3 e^-, and the corresponding energy levels provide insights into the available conductive channels at each charge state. The sequential electron capture behavior of C_{60} can be precisely controlled, driven by the coupling between electric field-regulated molecular vibrational modes and thermally activated electron transport. This work offers direct experimental evidence for a deeper understanding of fullerene-based materials as electron acceptors, specifically in their ability to sequentially capture, release, and transport electrons from a single-molecule perspective, opening up new opportunities for promising applications in quantum information science and molecular electronics.

ASSOCIATED CONTENT

Supporting Information

The Supporting Information is available free of charge at https://pubs.acs.org/doi/10.1021/jacs.5c08782.

Molecular synthesis, fabrication of graphene field-effect transistor arrays, molecular connection, statistical analysis of single-molecule connection, electrical characterization, bias-dependent current−time measurements of ME-C_{60} SMJs, bias-dependent current−time measurements of ME-Me_2 SMJs, temperature-dependent measurements of ME-C_{60} SMJs, theoretical calculations, and atomic coordinates for theoretical modeling (PDF)

AUTHOR INFORMATION

Corresponding Authors

Fanyang Mo − *School of Materials Science and Engineering, Peking University, Beijing 100871, P. R. China*; Email: fmo@pku.edu.cn

Zujin Shi − *Beijing National Laboratory for Molecular Sciences, National Biomedical Imaging Center, College of Chemistry and Molecular Engineering, Peking University, Beijing 100871, P. R. China*; orcid.org/0000-0003-0268-4584; Email: zjshi@pku.edu.cn

Jinying Wang − *Center of Single-Molecule Sciences, Institute of Modern Optics, Frontiers Science Center for New Organic Matter, Tianjin Key Laboratory of Micro-scale Optical Information Science and Technology, College of Electronic Information and Optical Engineering, Nankai University, Tianjin 300350, P. R. China*; Email: wangjynk@nankai.edu.cn

Chuancheng Jia − *Center of Single-Molecule Sciences, Institute of Modern Optics, Frontiers Science Center for New Organic Matter, Tianjin Key Laboratory of Micro-scale Optical Information Science and Technology, College of Electronic Information and Optical Engineering, Nankai University, Tianjin 300350, P. R. China*; Email: jiacc@nankai.edu.cn

Xuefeng Guo − *Beijing National Laboratory for Molecular Sciences, National Biomedical Imaging Center, College of Chemistry and Molecular Engineering, Peking University, Beijing 100871, P. R. China; Center of Single-Molecule Sciences, Institute of Modern Optics, Frontiers Science Center for New Organic Matter, Tianjin Key Laboratory of Micro-scale Optical Information Science and Technology, College of Electronic Information and Optical Engineering, Nankai University, Tianjin 300350, P. R. China*; orcid.org/0000-0001-5723-8528; Email: guoxf@pku.edu.cn

https://doi.org/10.1021/jacs.5c08782
J. Am. Chem. Soc. XXXX, XXX, XXX−XXX

Authors

Zezhou Yang − *Beijing National Laboratory for Molecular Sciences, National Biomedical Imaging Center, College of Chemistry and Molecular Engineering, Peking University, Beijing 100871, P. R. China*

Boyu Wang − *Center of Single-Molecule Sciences, Institute of Modern Optics, Frontiers Science Center for New Organic Matter, Tianjin Key Laboratory of Micro-scale Optical Information Science and Technology, College of Electronic Information and Optical Engineering, Nankai University, Tianjin 300350, P. R. China*

Xinmiao Xie − *Beijing National Laboratory for Molecular Sciences, National Biomedical Imaging Center, College of Chemistry and Molecular Engineering, Peking University, Beijing 100871, P. R. China*

Hanqiu Nie − *Beijing National Laboratory for Molecular Sciences, National Biomedical Imaging Center, College of Chemistry and Molecular Engineering, Peking University, Beijing 100871, P. R. China*

Jianning Zhang − *School of Materials Science and Engineering, Peking University, Beijing 100871, P. R. China*

Panfeng Chuai − *Beijing National Laboratory for Molecular Sciences, National Biomedical Imaging Center, College of Chemistry and Molecular Engineering, Peking University, Beijing 100871, P. R. China;* orcid.org/0009-0001-0579-2524

Jie Hao − *Beijing National Laboratory for Molecular Sciences, National Biomedical Imaging Center, College of Chemistry and Molecular Engineering, Peking University, Beijing 100871, P. R. China*

Wenlong Cai − *Beijing National Laboratory for Molecular Sciences, National Biomedical Imaging Center, College of Chemistry and Molecular Engineering, Peking University, Beijing 100871, P. R. China*

Zhiheng Yang − *Beijing National Laboratory for Molecular Sciences, National Biomedical Imaging Center, College of Chemistry and Molecular Engineering, Peking University, Beijing 100871, P. R. China*

Chunyan Gao − *Center of Single-Molecule Sciences, Institute of Modern Optics, Frontiers Science Center for New Organic Matter, Tianjin Key Laboratory of Micro-scale Optical Information Science and Technology, College of Electronic Information and Optical Engineering, Nankai University, Tianjin 300350, P. R. China*

Complete contact information is available at: https://pubs.acs.org/10.1021/jacs.5c08782

Author Contributions

[‖]Z.Y., B.W., X.X., H.N., and J.Z. contributed equally to this work.

Notes

The authors declare no competing financial interest.

■ ACKNOWLEDGMENTS

We acknowledge financial support from the National Key R&D Program of China (2023YFF1205803, 2022YFE0128700, 2024YFA1208100, 2021YFA1200102, and 2021YFA1200101), the National Natural Science Foundation of China (22173050), and Beijing National Laboratory for Molecular Sciences (BNLMS-CXXM-202407).

■ REFERENCES

(1) Mims, D.; Herpich, J.; Lukzen, N. N.; Steiner, U. E.; Lambert, C. Readout of spin quantum beats in a charge-separated radical pair by pump-push spectroscopy. *Science* **2021**, *374*, 1470−1474.

(2) Devir-Wolfman, A. H.; Khachatryan, B.; Gautam, B. R.; Tzabary, L.; Keren, A.; Tessler, N.; Vardeny, Z. V.; Ehrenfreund, E. Short-lived charge-transfer excitons in organic photovoltaic cells studied by high-field magneto-photocurrent. *Nat. Commun.* **2014**, *5*, 4529.

(3) García de Arquer, F. P.; Talapin, D. V.; Klimov, V. I.; Arakawa, Y.; Bayer, M.; Sargent, E. H. Semiconductor quantum dots: Technological progress and future challenges. *Science* **2021**, *373*, No. eaaz8541.

(4) Harris, R. D.; Bettis Homan, S.; Kodaimati, M.; He, C.; Nepomnyashchii, A. B.; Swenson, N. K.; Lian, S.; Calzada, R.; Weiss, E. A. Electronic processes within quantum dot-molecule complexes. *Chem. Rev.* **2016**, *116*, 12865−12919.

(5) Pan, F.; Ni, K.; Xu, T.; Chen, H.; Wang, Y.; Gong, K.; Liu, C.; Li, X.; Lin, M.; Li, S.; Wang, X.; Yan, W.; Yin, W.; Tan, P.; Sun, L.; Yu, D.; Ruoff, R. S.; Zhu, Y. Long-range ordered porous carbons produced from C_{60}. *Nature* **2023**, *614*, 95−101.

(6) Daisley, A.; Hargreaves, J. S. J. Fullerenes promote transition-metal-catalysed ammonia synthesis. *Nat. Chem.* **2024**, *16*, 1739−1740.

(7) Tan, Y.; Xie, S.; Huang, R.; Zheng, L. The stabilization of fused-pentagon fullerene molecules. *Nat. Chem.* **2009**, *1*, 450−460.

(8) Ai, Y.; Liao, W.; Weng, Y.; Lv, H.; Chen, X.; Song, X.; Li, P.; Xiong, R. Discovery of ferroelectricity in the fullerene adduct $C_{60}S_8$. *J. Am. Chem. Soc.* **2023**, *145*, 23292−23299.

(9) Baran, D.; Ashraf, R.; Hanifi, D. A.; Abdelsamie, M.; Gasparini, N.; Röhr, J. A.; Holliday, S.; Wadsworth, A.; Lockett, S.; Neophytou, M.; Emmott, C. J. M.; Nelson, J.; Brabec, C. J.; Amassian, A.; Salleo, A.; Kirchartz, T.; Durrant, J. R.; McCulloch, I. Reducing the efficiency-stability-cost gap of organic photovoltaics with highly efficient and stable small molecule acceptor ternary solar cells. *Nat. Mater.* **2017**, *16*, 363−369.

(10) Causa', M.; De Jonghe-Risse, J.; Scarongella, M.; Brauer, J. C.; Buchaca-Domingo, E.; Moser, J. E.; Stingelin, N.; Banerji, N. The fate of electron-hole pairs in polymer: fullerene blends for organic photovoltaics. *Nat. Commun.* **2016**, *7*, 12556.

(11) Zhang, Y.; Peng, X.; Tian, H.; Yang, B.; Chen, Z.; Li, J.; Zhang, T.; Zhang, M.; Liang, X.; Yu, Z.; Zhou, Y.; Zheng, L.; Wang, X.; Zheng, J.; Tang, Y.; Au, C.; Jiang, L.; Xie, S. Fullerene on non-iron cluster-matrix co-catalysts promotes collaborative H_2 and N_2 activation for ammonia synthesis. *Nat. Chem.* **2024**, *16*, 1781−1787.

(12) Hou, L.; Cui, X.; Guan, B.; Wang, S.; Li, R.; Liu, Y.; Zhu, D.; Zheng, J. Synthesis of a monolayer fullerene network. *Nature* **2022**, *606*, 507−510.

(13) Peng, B. Monolayer fullerene networks as photocatalysts for overall water splitting. *J. Am. Chem. Soc.* **2022**, *144*, 19921−19931.

(14) Chang, X.; Xu, Y.; von Delius, M. Recent advances in supramolecular fullerene chemistry. *Chem. Soc. Rev.* **2024**, *53*, 47−83.

(15) Hu, Z.; Yang, S. Endohedral metallofullerene molecular nanomagnets. *Chem. Soc. Rev.* **2024**, *53*, 2863−2897.

(16) Morton, J. J. L.; Tyryshkin, A. M.; Ardavan, A.; Benjamin, S. C.; Porfyrakis, K.; Lyon, S. A.; Briggs, G. A. D. Bang-bang control of fullerene qubits using ultrafast phase gates. *Nat. Phys.* **2006**, *2*, 40−43.

(17) Wu, J.; Peng, B. Smallest [5,6]fullerene as building blocks for 2D networks with superior stability and enhanced photocatalytic performance. *J. Am. Chem. Soc.* **2025**, *147*, 1749−1757.

(18) Utko, P.; Ferone, R.; Krive, I.; Shekhter, R.; Jonson, M.; Monthioux, M.; Noé, L.; Nygård, J. Nanoelectromechanical coupling in fullerene peapods probed by resonant electrical transport experiments. *Nat. Commun.* **2010**, *1*, 37.

(19) Pinto, D.; Paone, D.; Kern, B.; Dierker, T.; Wieczorek, R.; Singha, A.; Dasari, D.; Finkler, A.; Harneit, W.; Wrachtrup, J.; Kern, K. Readout and control of an endofullerene electronic spin. *Nat. Commun.* **2020**, *11*, 6405.

(20) Krachmalnicoff, A.; Bounds, R.; Mamone, S.; Alom, S.; Concistrè, M.; Meier, B.; Kouřil, K.; Light, M. E.; Johnson, M. R.; Rols, S.; Horsewill, A. J.; Shugai, A.; Nagel, U.; Rõõm, T.; Carravetta,

M.; Levitt, M. H.; Whitby, R. J. The dipolar endofullerene HF@C_{60}. *Nat. Chem.* **2016**, *8*, 953−957.
(21) Lu, S.; Zhang, Z.; Zhu, Y.; Tao, Y.; Lin, Q.; Zhang, Q.; Lv, X.; Hua, L.; Chen, Z.; Wang, H.; Zhuang, G.; Zhang, Q.; Guo, C.; Li, X.; Yu, X. Enhancing effect of fullerene guest and counterion on the structural stability and electrical conductivity of octahedral metallo-supramolecular cages. *Angew. Chem., Int. Ed.* **2024**, *63*, No. e202410710.
(22) Fang, H.; Chen, Q.; Lin, Y.; Xu, X.; Wang, J.; Li, M.; Xiao, C.; McNeill, C.; Tang, Z.; Lu, Z.; Li, W. Fullerene-hybridized fused-ring electron acceptor with high dielectric constant and isotropic charge transport for organic solar cells. *Angew. Chem., Int. Ed.* **2025**, *64*, No. e202417951.
(23) Yang, J.; Russell, J. C.; Tao, S.; Lessio, M.; Wang, F.; Hartnett, A. C.; Peurifoy, S. R.; Doud, E. A.; O'Brien, E. S.; Gadjieva, N.; Reichman, D. R.; Zhu, X.; Crowther, A. C.; Billinge, S. J. L.; Roy, X.; Steigerwald, M. L.; Nuckolls, C. Superatomic solid solutions. *Nat. Chem.* **2021**, *13*, 607−613.
(24) Hayakawa, M.; Sunayama, N.; Takagi, S. I.; Matsuo, Y.; Tamaki, A.; Yamaguchi, S.; Seki, S.; Fukazawa, A. Flattened 1D fragments of fullerene C_{60} that exhibit robustness toward multi-electron reduction. *Nat. Commun.* **2023**, *14*, 2741.
(25) Yang, C.; Chen, Z.; Yu, C.; Cao, J.; Ke, G.; Zhu, W.; Liang, W.; Huang, J.; Cai, W.; Saha, C.; Sabuj, M.; Rai, N.; Li, X.; Yang, J.; Li, Y.; Huang, F.; Guo, X. Regulation of quantum spin conversions in a single molecular radical. *Nat. Nanotechnol.* **2024**, *19*, 978−985.
(26) Park, H.; Park, J.; Lim, A. K. L.; Anderson, E. H.; Alivisatos, A. P.; McEuen, P. L. Nanomechanical oscillations in a single-C_{60} transistor. *Nature* **2000**, *407*, 57−60.
(27) Yang, C.; Li, Y.; Zhou, S.; Guo, Y.; Jia, C.; Liu, Z.; Houk, K. N.; Dubi, Y.; Guo, X. Real-time monitoring of reaction stereochemistry through single-molecule observations of chirality-induced spin selectivity. *Nat. Chem.* **2023**, *15*, 972−979.
(28) Yu, L. H.; Natelson, D. The kondo effect in C_{60} single-molecule transistors. *Nano Lett.* **2004**, *4*, 79−83.
(29) Roch, N.; Florens, S.; Bouchiat, V.; Wernsdorfer, W.; Balestro, F. Quantum phase transition in a single-molecule quantum dot. *Nature* **2008**, *453*, 633−637.
(30) Winkelmann, C. B.; Roch, N.; Wernsdorfer, W.; Bouchiat, V.; Balestro, F. Superconductivity in a single-C_{60} transistor. *Nat. Phys.* **2009**, *5*, 876−879.
(31) Zheng, X.; Lu, W.; Abtew, T. A.; Meunier, V.; Bernholc, J. Negative differential resistance in C_{60}-based electronic devices. *ACS Nano* **2010**, *4*, 7205−7210.
(32) Lau, C.; Sadeghi, H.; Rogers, G.; Sangtarash, S.; Dallas, P.; Porfyrakis, K.; Warner, J.; Lambert, C. J.; Briggs, G. A. D.; Mol, J. A. Redox-dependent Franck−Condon blockade and avalanche transport in a graphene−fullerene single-molecule transistor. *Nano Lett.* **2016**, *16*, 170−176.
(33) Bai, J.; Li, X.; Zhu, Z.; Zheng, Y.; Hong, W. Single-molecule electrochemical transistors. *Adv. Mater.* **2021**, *33*, 2005883.
(34) Nichols, R. J.; Higgins, S. J. Single molecule nanoelectrochemistry in electrical junctions. *Acc. Chem. Res.* **2016**, *49*, 2640−2648.
(35) Ward, J. S.; Vezzoli, A. Key advances in electrochemically-addressable single-molecule electronics. *Curr. Opin. Electrochem.* **2022**, *35*, 101083.
(36) Zhang, K.; Wang, C.; Zhang, M.; Bai, Z.; Xie, F.; Tan, Y.; Guo, Y.; Hu, K.; Cao, L.; Zhang, S.; Tu, X.; Pan, D.; Kang, L.; Chen, J.; Wu, P.; Wang, X.; Wang, J.; Liu, J.; Song, Y.; Wang, G.; Song, F.; Ji, W.; Xie, S.; Shi, S.; Reed, M. A.; Wang, B. A Gd@C_{82} single-molecule electret. *Nat. Nanotechnol.* **2020**, *15*, 1019−1024.
(37) Li, J.; Hou, S.; Yao, Y.; Zhang, C.; Wu, Q.; Wang, H.; Zhang, H.; Liu, X.; Tang, C.; Wei, M.; Xu, W.; Wang, Y.; Zheng, J.; Pan, Z.; Kang, L.; Liu, J.; Shi, J.; Yang, Y.; Lambert, C. J.; Xie, S.; Hong, W. Room-temperature logic-in-memory operations in single-metallofullerene devices. *Nat. Mater.* **2022**, *21*, 917−923.
(38) Gehring, P.; Harzheim, A.; Spiece, J.; Sheng, Y.; Rogers, G.; Evangeli, C.; Mishra, A.; Robinson, B. J.; Porfyrakis, K.; Warner, J. H.; Kolosov, O. V.; Briggs, G. A. D.; Mol, J. A. Field-effect control of graphene−fullerene thermoelectric nanodevices. *Nano Lett.* **2017**, *17*, 7055−7061.
(39) Meisner, J. S.; Ahn, S.; Aradhya, S. V.; Krikorian, M.; Parameswaran, R.; Steigerwald, M.; Venkataraman, L.; Nuckolls, C. Importance of direct metal−π coupling in electronic transport through conjugated single-molecule junctions. *J. Am. Chem. Soc.* **2012**, *134*, 20440−20445.
(40) Zuev, P. S.; Sheridan, R. S.; Albu, T. V.; Truhlar, D. G.; Hrovat, D. A.; Borden, W. T. Carbon tunneling from a single quantum state. *Science* **2003**, *299*, 867−870.
(41) Michel, C. S.; Lampkin, P. P.; Shezaf, J. Z.; Moll, J. F.; Castro, C.; Karney, W. L. Tunneling by 16 carbons: Planar bond Shifting in [16]annulene. *J. Am. Chem. Soc.* **2019**, *141*, 5286−5293.
(42) Zhu, X.; Wang, B.; Xiong, W.; Zhou, S.; Qu, K.; Lü, J.; Chen, H.; Jia, C.; Guo, X. Vibration-assisted charge transport through positively charged dimer junctions. *Angew. Chem., Int. Ed.* **2022**, *61*, No. e202210939.
(43) Zhang, M.; Wang, B.; Jia, H.; Xie, X.; Hao, J.; Zhou, L.; Du, P.; Wang, J.; Jia, C.; Guo, X. Dual-vibration-assisted charge transport through hexabenzocoronene in single-molecule junctions. *Adv. Sci.* **2025**, *12*, 2408310.
(44) Yang, C.; Liu, Z.; Li, Y.; Zhou, S.; Lu, C.; Guo, Y.; Ramirez, M.; Zhang, Q.; Li, Y.; Liu, Z.; Houk, K. N.; Zhang, D.; Guo, X. Electric field−catalyzed single-molecule Diels-Alder reaction dynamics. *Sci. Adv.* **2021**, *7*, No. eabf0689.

https://doi.org/10.1021/jacs.5c08782
J. Am. Chem. Soc. XXXX, XXX, XXX−XXX